

Coupled Aeropropulsive Design Optimization of a 3-D BLI Propulsor Considering Inlet Distortion

Justin S. Gray *

NASA Glenn Research Center, Cleveland, OH, 44135

Charles A. Mader[†],

Department of Aerospace Engineering, University of Michigan, Ann Arbor, MI, 48109

Gaetan K. W. Kenway[‡],

Science and Technology Corporation, Moffett Field, CA, 94035

Joaquim R. R. A. Martins[§]

Department of Aerospace Engineering, University of Michigan, Ann Arbor, MI, 48109

Boundary layer ingestion (BLI) promises increased aircraft efficiency, but excessive inlet distortion must be avoided to prevent fans that are too heavy or structurally infeasible. We propose a new approach to study the effect of distortion on BLI propulsors via an aeropropulsive design optimization with a constraint on inlet distortion using highly efficient gradient-based methods with analytic derivatives. The fully coupled aeropropulsive model includes a 3-D RANS aerodynamic analysis of the flow and a thermodynamic cycle model of the propulsor fan. We minimize the shaft power required at cruise for the aft BLI thruster by varying the propulsor size and the shape of the propulsor nacelle and aft fuselage. Optimizations are performed with and without the inlet distortion constraint for different aft propulsor sizes to study the impact of the constraint on overall BLI performance. The results show that imposing a distortion constraint increased the required propulsor shaft power by up to 1.2% relative to the unconstrained case, and that smaller propulsors suffer lower performance degradation than larger ones. The results underline the importance of using a fully-coupled aeropropulsive model to predict BLI performance and demonstrate the power of aeropropulsive optimization in the design of BLI configurations.

Nomenclature

A = area

C_F = force coefficient

* Aerospace Engineer, PSA Branch, 21000 Brookpark Rd., MS 5-11, 44135; Member AIAA

[†] Assistant Research Scientist, 1320 Beal Ave, Ann Arbor, MI 48109; Senior Member AIAA

[‡] Aerospace Engineer, Moffett Field, CA 94035; Senior Member AIAA

[§] Professor, 1320 Beal Ave, Ann Arbor, MI 48109; Fellow AIAA

C_L	=	lift coefficient
F	=	force
FPR	=	fan pressure ratio
\vec{f}_{visc}	=	surface force per unit area
g_{geo}	=	geometric thickness of the nacelle relative to the baseline
\dot{m}	=	mass flow rate
M	=	Mach number
\hat{n}	=	vector normal to a surface
NPR	=	nozzle pressure ratio
p	=	pressure
P	=	fan shaft power required for propulsor
PSC	=	power saving coefficient
R	=	ideal gas constant
\mathcal{R}	=	residual
S	=	entropy
V	=	air velocity
X	=	shape design variables for optimization
α	=	angle of attack
η	=	efficiency
κ	=	ARP1420 distortion metric
$\hat{\kappa}$	=	aggregated ARP1420 distortion metric
ρ	=	air density
θ	=	angular position on the fan face

Superscripts

prop	=	values defined in the propulsion model
ff	=	values computed on the plane of the fan face
$\bar{()}$	=	average quantity

Subscripts

BLI	=	quantity defined for a BLI propulsor
in	=	flow entering the fan
net	=	quantity integrated over the entire aircraft surface
out	=	flow leaving the fan

ref	=	reference quantity
s	=	static thermodynamic quantity
t	=	total thermodynamic quantity
∞	=	freestream value

I. Introduction

Recently, there has been a resurgence of interest in boundary layer ingestion (BLI) as a way to increase aircraft efficiency. This resurgence has been motivated in part by developments in electric propulsion systems, which provide more flexibility in the location and number of propulsors. BLI for aircraft applications was first proposed by Smith and Roberts [1] in a 1947 paper that studied the use of jet intakes embedded in the boundary layer as a means to maintain laminar flow and reduce aircraft drag. Aircraft applications for BLI were not examined in further detail initially, but the idea was studied under the term “wake ingestion” for marine applications in the 1960’s [2, 3]. Much later, a 1993 paper by Smith [4] combined boundary layer analysis with basic propulsion modeling to show the potential for significant fuel burn reduction. Inlet distortion and its effect on BLI performance is a notable topic missing from all of this early research. Distortion, if not accounted for in the design of a BLI propulsor, will at best partially offset the BLI benefit, and at worst, cause structural failure of the propulsor fan blades. More recent work examined the impact of inlet distortion both computationally [5, 6] and through a wind tunnel test of a fan designed specifically for highly distorted flow [7–10]. The early work considered the sizing of BLI propulsors, and the later work examined the effects of distortion on a fixed size propulsor. The aim of this work is to consider both issues at the same time and to evaluate the impact of distortion across a range of BLI propulsor sizes. We examine a series of optimized BLI propulsors for NASA’s STARC-ABL aircraft concept [11] for three propulsor sizes with and without a constraint on allowable inlet distortion.

The fully coupled aeropropulsive analysis used in this work poses a fundamental book keeping problem. Smith [4] stated that for BLI applications, thrust and drag are not separable quantities, as assumed in the classical definition of propulsive efficiency. When using this classical definition, the propulsive efficiency of BLI can be greater than one, making it an ill-defined metric in this case [12, pp. 215–217]. Smith developed an alternative power-based metric to evaluate the performance of BLI propulsion called the power saving coefficient (PSC), which is defined as

$$\text{PSC} = \frac{P - P_{\text{BLI}}}{P}. \quad (1)$$

This metric captures the relative difference between the propulsive power required for an aircraft at a given operating condition with BLI (P_{BLI}) to an aircraft without BLI (P). Smith [4] predicted PSC values in the range of 0.1 to 0.5, corresponding to a reduction between 10% and 50% in the propulsive power required with BLI.

Further work by Drela [13] proposed a unified power balance accounting scheme that allowed the calculation of the

power saving coefficient in a consistent and well-defined manner for a combination of airframe and propulsion systems. The crucial insight from the work of Betz, Smith, and Drela is that traditional thrust-drag based accounting schemes do not work well in coupled aeropropulsive problems and that power-based accounting methods are more appropriate. Therefore, instead of optimizing for traditional performance metrics like thrust and drag, we focus on the shaft power required for the propulsor instead. Since 2000, a number of conceptual design studies have examined the aircraft-level benefits of BLI propulsion systems considering a wide range of fuselage and propulsor configurations [11, 14–20].

All of these system-level studies were performed with uncoupled models the BLI system. We consider the models to be “uncoupled” when the coupling between the aerodynamic and propulsion models is only in one direction, as defined by Hendricks [21]. Hendricks notes that the direction of communication is not important; fixed inlet flow conditions can be passed from the aerodynamic model or fixed propulsion boundary conditions can be passed from the propulsion model. As long as the communication is unidirectional, then we consider the models uncoupled because they lack the feedback necessary to capture the full aeropropulsive interaction.

NASA’s STARC-ABL configuration, first proposed by Welstead and Felder [11], is relatively conventional compared to other configurations. As shown in Fig. 1, it is a tube-with-wings configuration that uses an aft-mounted electrically-powered BLI propulsor in conjunction with two traditional under-wing engines. Like other conceptual design studies, Welstead and Felder [11] used an uncoupled analysis for the propulsor. All of these studies neglected the impact of inlet distortion on the BLI performance, or accounted for it only indirectly via a small decrement to fan-efficiency.

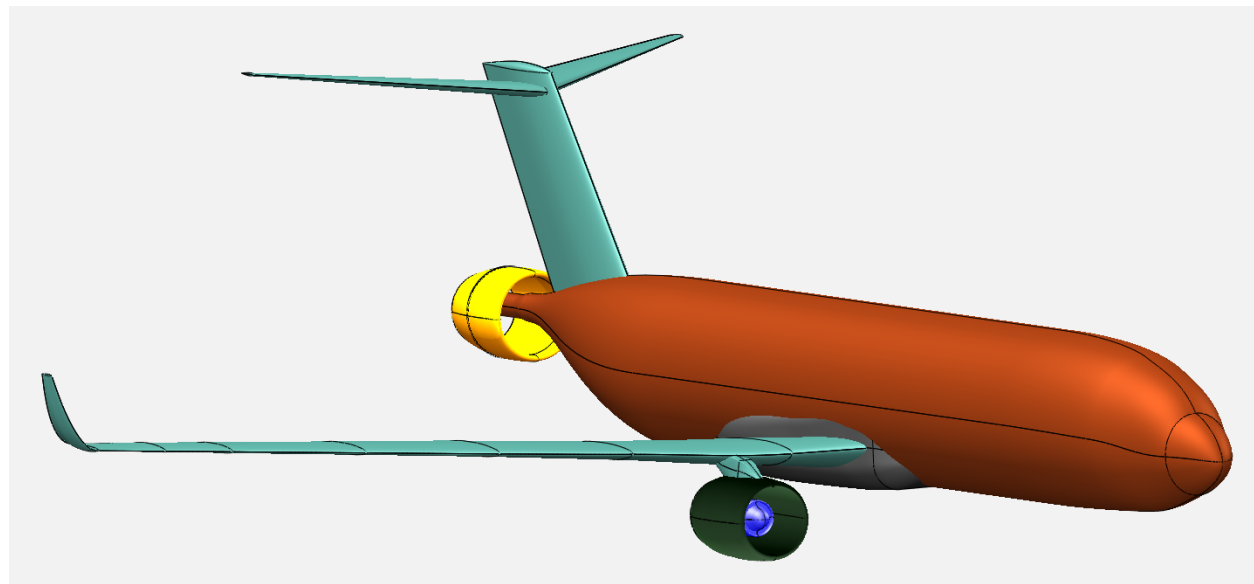


Fig. 1 STARC-ABL aircraft geometry including the vertical tail and aft-mounted BLI propulsor.

In our prior work, we demonstrated the importance of using a fully-coupled aeropropulsive model—versus an uncoupled model—to predict BLI performance [22, 23]. The coupled model predicts different propulsor inlet conditions and a different surface pressure distribution on the fuselage. These effects dominate the overall performance predictions

for BLI [22]. The analysis in that work was performed on a simplified 2-D geometry based on the STARC-ABL configuration.

In a follow-up study using that 2-D geometry and the fully coupled aeropropulsive model, we performed a design study focused on sizing the propulsor using gradient-based optimization [23]. Those results showed that the BLI system offered reductions between 1% and 4.6% in total power required for cruise, depending on the assumption made about the power transmission efficiency of the turboelectric system. The variation of system-level performance with transmission efficiency—which governs how much power is lost by moving it from under-wing generators to the aft mounted propulsor—established it as a key design assumption for the BLI system. These two papers predicted a significantly smaller BLI performance benefit than the original prediction of 12% by Welstead and Felder [11], but the new results were based on a more rigorous power-based accounting scheme and fully coupled aeropropulsive models. Subsequent results by Bowman et al. [24] re-examined the original calculations by Welstead and Felder and revised their prediction down to a 3.4% improvement over the baseline. This was due to a more complete force accounting scheme that included previously missed ram drag effects. The updated results of Bowman et al. corroborate the results by the authors. However, a separate study by Hall et al. [25] that used Drela’s power balance scheme found that the STARC-ABL concept sized by Welstead and Felder would perform 5% worse than a conventional baseline. By shrinking the after propulsor significantly, Hall et al., found they could reduce that figure to 0.5% worse than the baseline, but it was still worse. This large spread in the predictions from various studies serves to underscore the need for fully-coupled analysis to reduce the potential sources of discrepancy.

Recent aerodynamic analysis of the STARC-ABL configuration has clearly shown that 3-D aerodynamic models are necessary to accurately predict the airflow over the aft fuselage and to capture inlet distortion effects. Rodriguez [26] reached similar conclusions by using a combination of 2-D and 3-D aerodynamic models to perform the first shape optimization of a BLI propulsor for a blended-wing-body configuration. He showed that 2-D models were insufficient when applying a distortion constraint. Recent wind tunnel tests of a BLI configuration have confirmed that inlet flow distortion is a prominent feature in BLI applications and that accounting for it in the fan design is an important practical consideration in terms of BLI system performance and structural design [8]. Distortion can lower turbomachinery efficiency and lead to reduced life for turbomachinery due to large cyclic structural loadings. In the extreme, distortion could lead to fan blade structural failure. Therefore, it is important to have a design capability that can address distortion, which requires full 3-D, non-axisymmetric, aeropropulsive modeling.

Rodriguez [26, 27] treated inlet distortion as a constraint and concluded that the aerodynamic design variables he used could only reduce distortion by a small amount for the blended-wing-body configuration he considered. Later, in two independent studies—Ordaz et al. [5] and Kenway and Kiris [6]—sought to minimize inlet distortion for aft BLI thrusters with aerodynamic shape optimizations (i.e., they used distortion as the objective function) and had more success in reducing the distortion levels relative to the baseline. Kenway and Kiris [6] identified two causes of distortion

at the propulsor fan face: the non-axisymmetric fuselage and the wing downwash. Their results showed that the fuselage geometry causes minor flow asymmetry, but that the wing downwash contributed much more to the distortion. In the all the work cited above, the propulsor size was always fixed and the fan design (i.e., the FPR) was also fixed.

Given the non-axisymmetric nature of the flow over the aft propulsor of the STARC-ABL concept, it is reasonable to assume that distortion varies with changes in the BLI propulsor size, which in turn affects the performance. This variation is in addition to the inherent changes in BLI propulsor performance as it changes size and ingests more or less of the boundary layer. All of these confounding factors beg the question: How should the thrust split between the under-wing engines and aft-propulsor be determined? Answering this question is key to performing sizing studies for a STARC-ABL aircraft because the relative size of the two propulsion sub-systems is a critical design decision.

Motivated by the need to consider both distortion and aft propulsor size, we present an aeropropulsive design optimization of the STARC-ABL BLI propulsor that includes both aerodynamic and propulsion design variables. Similar to prior work, the optimization is performed using gradient-based optimization combined with a fully-coupled aeropropulsive model. The models used in this work are built with the OpenMDAO framework [28], which enables the computation of derivatives for the fully-coupled model. A key difference in this work compared to the previous distortion studies is the inclusion of propulsion design variables and a large variation in propulsor sizing for the final optimized results. We use a body-force model in the aerodynamic analysis [18, 29] to model the aft-propulsor thrust and a separate thermodynamic cycle analysis to model the propulsor shaft power. This splits the physical system into two disciplinary models, which is a new approach to coupled aeropropulsive modeling and one of the primary contributions of this work. The aerodynamic and propulsion models are detailed in Secs. II and III, respectively. The results from this design study are the first to provide a quantitative analysis of the impact of fan distortion on BLI propulsor sizing and constitute another primary contribution of this paper. The optimization problem formulation and corresponding results are presented in Sec. IV.

II. Aerodynamic Model

A. Aircraft Geometry

The STARC-ABL geometry shown in Fig. 1 is modeled with the OpenVSP geometry engine [30], which outputs a surface discretization for each component in the mesh individually. A rigid link interpolation scheme is used to connect the OpenVSP surface discretization to the surface discretization of the computational fluid dynamics (CFD) mesh. Changes in the surface CFD mesh are propagated to the volume mesh via an inverse distance weighting implementation of mesh-morphing [31].

Figure 2 illustrates the shape parameterization for the aft-fuselage and BLI propulsors. OpenVSP defines surfaces using Bézier curves, which for the fuselage and nacelle are parameterized using cross sections to define surface radii and

then local tangent strength and angle to define surface curvature. The red cross sections represent elliptical shapes with independent control of height and width. The yellow cross sections indicate circular shapes, which are parameterized using a single diameter variable. In addition to separate control over each cross section, there is also a global design variable for the nacelle diameter that scales all the cross sections together. A total of 25 shape variables is used to define the surface of the aft-fuselage, nacelle, and nozzle plug.

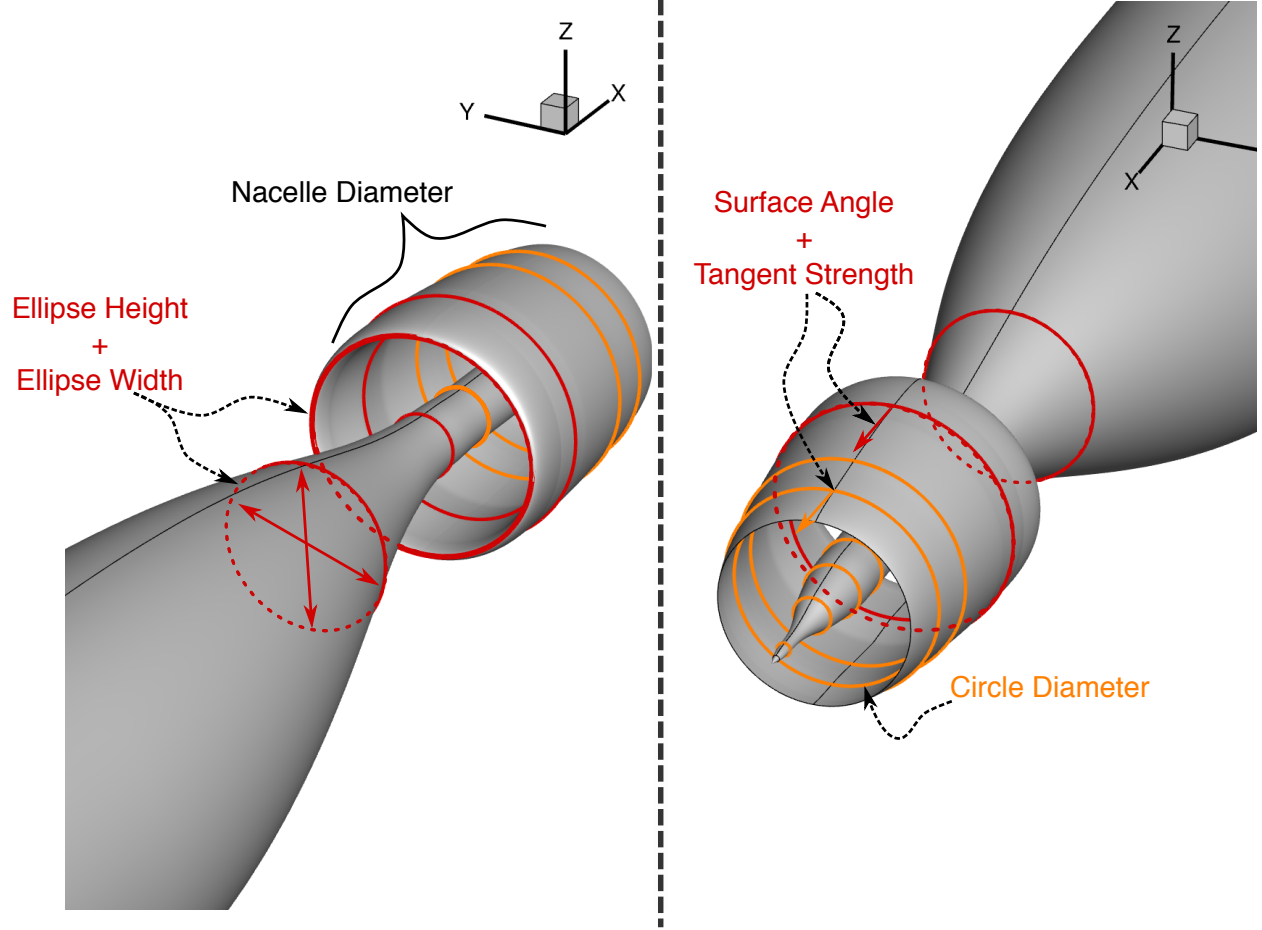


Fig. 2 Location of cross sections and shape parameterization types used to define the aft propulsor geometry in OpenVSP.

B. CFD Solver: ADflow

For the aerodynamic analysis, we use the open-source CFD solver ADflow [32].* ADflow uses an approximate Newton–Krylov approach to solve the Reynolds averaged Navier Stokes (RANS) equations [33] and it includes an adjoint implementation that efficiently computes derivatives for gradient-based optimization [34]. The overset meshes are generated using the Chimera Grid Tools [35] and an implicit hole cutting scheme [31]. The mesh—shown in Fig. 3—is composed of eight different sub-meshes for a total of 6 million cells.

*<https://github.com/mdolab/adflow>

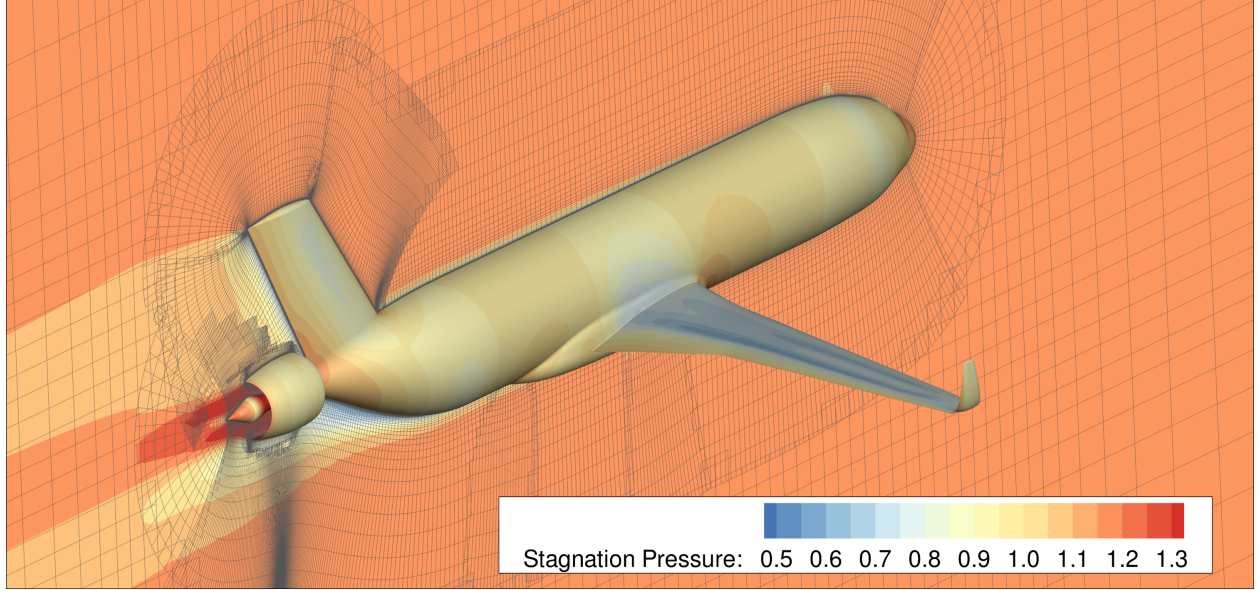


Fig. 3 Overset mesh of the model showing the surface C_p contours for the nominal cruise flight condition.

The aircraft wing was optimized for minimum drag in prior work using a 5-point multipoint stencil around the nominal cruise condition ($M = 0.785$ at 37,000 ft). The wing geometry is held fixed at this previously optimized design for all studies performed in this work. The BLI propulsor is modeled using a body-force zone [29, 36, 37], which imparts the effect of the fan on the flow without needing to model the fan itself. The effect of the body-force zone is highlighted in Fig. 4, where the contours of total pressure indicate the pressure rise that captures the effect of the fan.

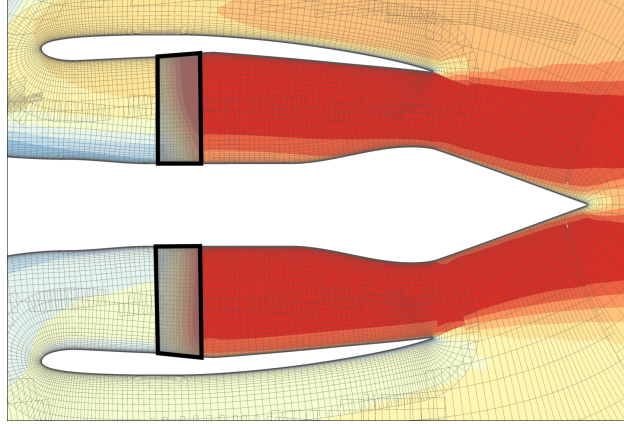


Fig. 4 Side view of the BLI propulsor, including the body-force zone, where the color contours show the increased total pressure after the fan.

C. Mesh Convergence Study

A mesh convergence study is performed to verify the model convergence properties. This study considers three different mesh refinement levels: coarse, medium, and fine, with roughly 6 million, 17 million, and 49 million

cells, respectively. All the analyses for this mesh convergence study are done for the baseline aft fuselage geometry with the pre-optimized wing shape. Richardson extrapolation estimates of the continuum value for two key metrics are performed to show that the model converges to a reasonable value as the mesh spacing is decreased. The optimizations performed in this work were done using the coarsest mesh (6 million cells), to achieve a reasonable computational cost.

Mesh convergence results for the net force coefficient (C_F) are shown in Fig. 5, which result in a continuum value of 66 force counts. We also examine the distortion metric to ensure that this new aerodynamic functional also has good convergence properties. Figure 6 shows that the Richardson extrapolation predicts a continuum value of 0.04255 for the aggregated distortion metric (\hat{k}). These convergence studies show second order convergence behavior, which is expected given the second-order finite-volume scheme used in ADflow. The calculation of the aggregated distortion metric is detailed in Sec. IV; Fig. 6 shows that it does converge as expected as the mesh is refined.

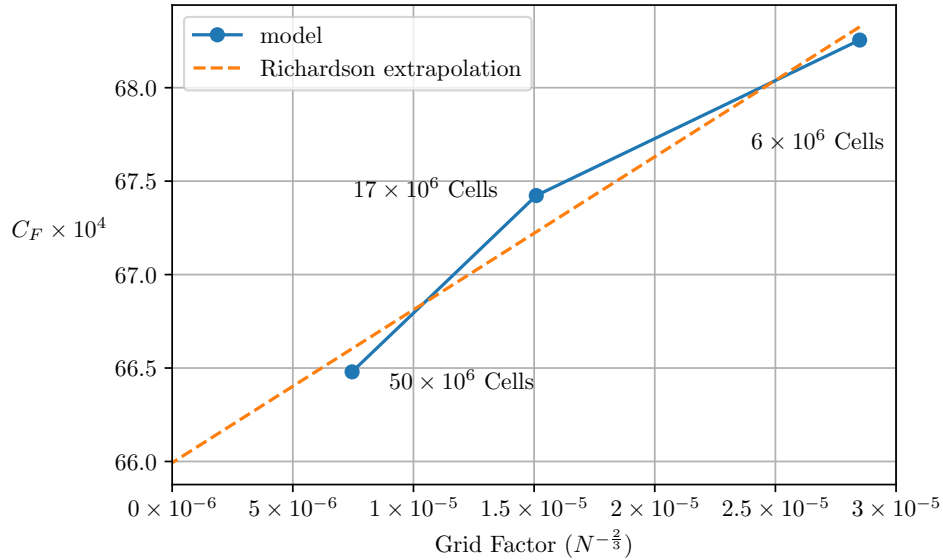


Fig. 5 Net force coefficient mesh convergence study for the 3-D STARC-ABL aerodynamic model.

D. Force Accounting

In conventional aircraft designs, the fluid domain can usually be separated into internal and external flows, which is convenient for bookkeeping. Surfaces exposed to external flow, (such as wings, nacelles, and fuselage) count towards drag, while surfaces immersed in internal flow (such as engine walls) count towards thrust. Unfortunately, this distinction breaks down for BLI because there are aerodynamic surfaces that are exposed to both internal and external flows (such as the aft fuselage of the STARC-ABL configuration), justifying the need for a different approach.

In this work, when forces are required, thrust-drag components are not separated. Instead, a signed force (or force coefficient) is computed by integrating pressure and viscous forces on all the walls in the aerodynamic model and then adding the force contribution from the body-force zone [29]. This additional force represents the effect of the fan inside

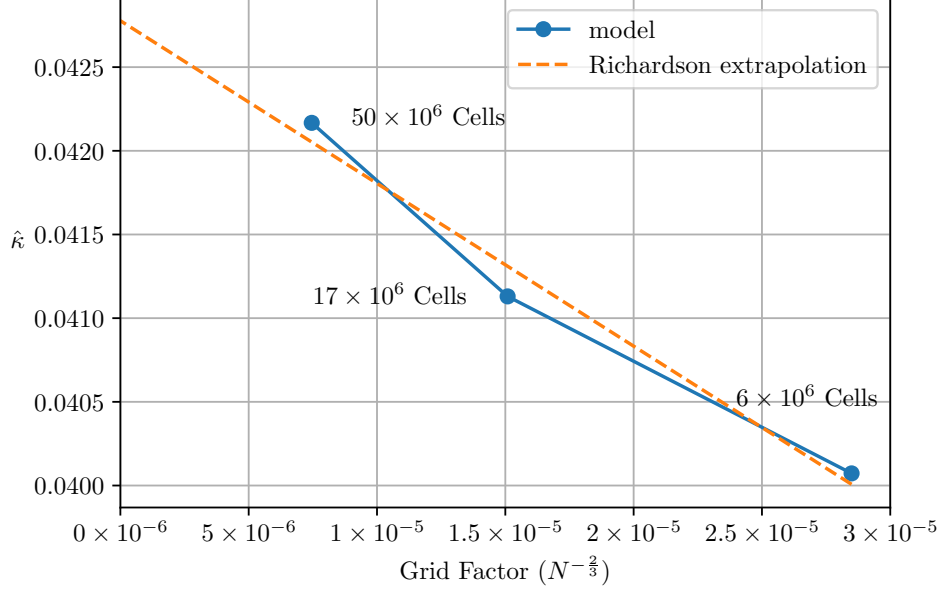


Fig. 6 Aggregated distortion metric mesh convergence study for the 3-D STARC-ABL aerodynamic model.

the CFD model (see Fig. 4). The total force coefficient on the aircraft is computed by:

$$C_F = \frac{2}{\rho_\infty V_\infty^2 A_{\text{ref}}} \left[\iint_S \left((p - p_\infty) \hat{n} + \vec{f}_{\text{visc}} \right) dS + (\vec{F}_{\text{BLI}} \cdot \hat{n}_{\text{BLI}}) \right], \quad (2)$$

where F_{BLI} represents the force contribution from the body-force zone in the aft propulsor. This is not the same as the net thrust from that propulsor, but rather, it is the net force that would be felt by the fan itself. The integration surface, S , is composed of every wall of the airframe: wing, tail, fuselage, and the inside and outside of the propulsor nacelle. The net force coefficient, C_F , corresponds to force on the entire wing-fuselage-tail-propulsor system and is a signed quantity. A positive value indicates deceleration, while a negative value indicates acceleration. This net force does not include the contribution from the under-wing propulsor because they are not modeled in this work. For a cruise condition with a constant velocity, the net force coefficient of the entire aircraft should be zero, but here C_F is a positive quantity that represents the required force coefficient that must be generated by the under-wing engines to reach a steady cruise condition.

III. Propulsion Model

A. Conservative Aeropropulsive Transfer

The thermodynamic cycle propulsion model requires scalar flow quantities as inputs, but the aerodynamic analysis computes the flow quantities as a nonuniform distribution over a 2-D plane that serves as the interface between the two models. The 2-D data needs to be averaged in a conservative fashion so that the correct net force on the boundary is

retained in both analyses.

There are a number of different approaches to do this averaging while conserving the flow quantities. Livesey and Hugh [38] and Livesey [39] compared a number of different methods for the purpose of computing scalar values from experimental rake data. They concluded that an entropy-conserving approach was the most useful in that context because it ensured physically meaningful pressure loss coefficients when the averaged values are compared at multiple axial locations. However, this approach does not preserve momentum flux in the axial direction.

In our application, the interface plane represents a transition from one analysis to another at a single axial location. We seek to have the same net force on the interface plane between the two analyses. The force is determined by the static pressure and the momentum flux through the interface plane, so these are the quantities we seek to conserve. Typically in cycle analysis tools, all performance calculations are based on the total properties of the flow so matching static properties may seem nonintuitive, but the choice is based on the desire to have consistent momentum flux across the interface plane. In the aerodynamic analysis, the force normal to any plane is computed by

$$F_S = \iint_S \left[(p_s - p_\infty) + \rho(\vec{V} - \vec{V}_\infty) \cdot \hat{n}(\vec{V} \cdot \hat{n}) \right] dS. \quad (3)$$

If we assume uniform values across the plane, so that the flow can be represented by scalar values, this simplifies to

$$F_S = \left[(\bar{p}_s - p_\infty)A + \dot{m}(\vec{V} - \vec{V}_\infty) \cdot \hat{n} \right]. \quad (4)$$

Over any given plane, the total mass flow rate and area are

$$\dot{m} = \iint_S \rho \vec{V} \cdot \hat{n} dS, \quad (5)$$

$$A = \iint_S dS. \quad (6)$$

Equating Eqs. (3) and (4), canceling out the p_∞ and V_∞ terms, and separating the pressure and velocity components yields

$$\bar{p}_s = \frac{1}{A} \iint_S p_s dS, \quad (7)$$

$$\vec{V} = \frac{1}{\dot{m}} \iint_S \rho(\vec{V} \cdot \hat{n})^2 dS. \quad (8)$$

These two equations show that the force-conserving averaging scheme of the propulsion model inflow conditions should be chosen such that the static pressure matches the area-averaged static pressure and that the flow velocity should match the mass-averaged velocity on the interface plane. To ensure this, we solve for the propulsor inlet total

pressure (p_t^{prop}), total temperature (T_t^{prop}), and Mach number (M^{prop}), such that the static properties in the propulsion model matches averaged aerodynamic model quantities given by Eqs. (6), (7), and (8). Thus, the following three residual equations must be satisfied to ensure that we have a force-conserving data transfer between the aerodynamic and propulsion models:

$$\mathcal{R}_p(\dot{m}, M^{\text{prop}}, T_t^{\text{prop}}, p_t^{\text{prop}}) = p_s^{\text{prop}} - \bar{p}_s = 0 \quad (9)$$

$$\mathcal{R}_T(\dot{m}, M^{\text{prop}}, T_t^{\text{prop}}, p_t^{\text{prop}}) = V^{\text{prop}} - \bar{V} = 0 \quad (10)$$

$$\mathcal{R}_M(\dot{m}, M^{\text{prop}}, T_t^{\text{prop}}, p_t^{\text{prop}}) = A^{\text{prop}} - A = 0 . \quad (11)$$

The mass flow (5) computed by the aerodynamic model is used as a direct input to the propulsion model, which provides the last value needed to fully describe the thermodynamic cycle propulsion model flow state.

A consequence of this force-conserving scheme is that, while the static properties match between the aerodynamic and propulsion codes (by design), the equivalent averaged total properties are not guaranteed to match each other. Total properties do not exist in a concrete form in the real world, but instead represent an accounting scheme to track the total energy and momentum of the flow in terms of thermodynamic properties. Thus, the exact values for the total properties are highly dependent on the exact thermodynamic model used by the aerodynamic and propulsion codes. If the two codes use different thermodynamic models, then the total properties will not match. In this work, the aerodynamic model assumes a constant ratio of specific heats (γ) and the propulsion model uses a more detailed model where γ is not constant [40]. Therefore, the total properties will not match exactly.

B. BLI Propulsor Model

Although the force from the BLI propulsor is modeled via a body-force zone in the aerodynamics model, a propulsion model is still needed to compute the shaft power required to produce that force, accounting for the fan adiabatic efficiency. The propulsion model is a thermodynamic cycle model built with the propulsion modeling library pyCycle [41, 42]. pyCycle provides a modular environment to construct any propulsion system by building up a model from a set of “elements” (e.g., inlet, compressor, nozzle). pyCycle was chosen because it can efficiently compute analytic derivatives for propulsion models, which is crucial for the gradient-based optimization algorithm used here. This BLI propulsor model is composed of four cycle elements: *Flow Start*, *Fan*, *Atmosphere*, and *Performance*. The dependencies between these elements are shown in Fig. 7 using an extended design structure matrix [43]. A Newton solver is used to converge the implicit relationships within the model.

The *CFD Start* element relies on the Newton solver to implement the force-conserving force transfer scheme described in Sec. III.A. The *Atmosphere* element uses the U.S. Standard Atmosphere 1976 [44] to compute the freestream flow properties. The *Fan* and *Performance* elements include the thermodynamic model that computes the required shaft

power, given the \dot{m} and the fan pressure ratio (FPR) computed by the aerodynamic analysis and the assumed power transmission efficiency η_{trans} . Figure 7 shows the connections between the four cycle elements of this model.

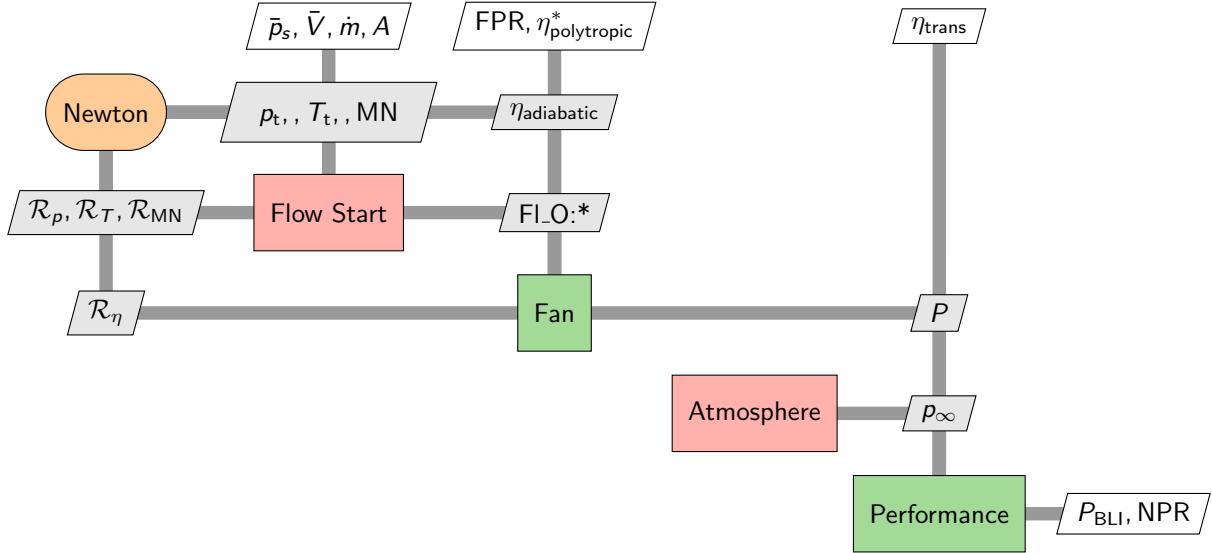


Fig. 7 XDSM for the pyCycle BLI Fan model showing cycle elements in the propulsor model. Green elements use explicit calculations, red elements use implicit calculations.

The model assumes a constant 97% fan polytropic efficiency ($\eta_{\text{polytropic}}$), which matches the technology assumptions for NASA's N+3 high bypass ratio turbofan engine [45]. However, to enforce that assumption requires an additional implicit residual equation because in pyCycle, the fan shaft power is a function of adiabatic efficiency ($\eta_{\text{adiabatic}}$). Furthermore, given $\eta_{\text{adiabatic}}$, the model computes changes in entropy across the compressor, which it uses to compute $\eta_{\text{polytropic}}$ as follows:

$$\eta_{\text{polytropic}} = \frac{R \ln(\text{FPR})}{R \ln(\text{FPR}) + S_{\text{out}} - S_{\text{in}}}. \quad (12)$$

Thus, in order to have a model with constant $\eta_{\text{polytropic}}$, we use Eqn. 12 to formulate the residual,

$$\mathcal{R}_{\eta}(\text{FPR}, \eta_{\text{adiabatic}}) = \left[\frac{R \ln(\text{FPR})}{R \ln(\text{FPR}) + S_{\text{out}} - S_{\text{in}}} \right] - \eta_{\text{polytropic}}^* = 0, \quad (13)$$

where $\eta_{\text{polytropic}}^*$ is the target constant polytropic efficiency of 97%, keeping in mind that the entropy terms are themselves implicitly related to both FPR and $\eta_{\text{adiabatic}}$. The Newton solver in the propulsion model converges this additional residual, along with all other residuals in the model.

The effect of holding a constant $\eta_{\text{polytropic}}$ is that $\eta_{\text{adiabatic}}$ —the quantity that directly impacts the shaft power—varies with respect to FPR and is always less than 97%. Although we endeavored to capture this effect, it is extremely small when considering the narrow FPR range observed in practice and when the assumption of constant $\eta_{\text{polytropic}}$ becomes

less valid for larger changes in FPR. In the final results, the optimized FPR varied between 1.2 and 1.3 and the computed $\eta_{\text{adiabatic}}$ was held constant at 0.969 when rounded to the third decimal place. In future work, it would be acceptable to assume a constant $\eta_{\text{adiabatic}}$, based on an offline calculation.

This model outputs the required generator power (P_{BLI}) and the nozzle pressure ratio (NPR), which takes into account $\eta_{\text{adiabatic}}$ and the power transmission efficiency (η_{trans}). The objective of the optimization is to minimize P_{BLI} subject to an NPR constraint.

IV. Aeropropulsive Optimization

A. Optimization Problem

The performance of the BLI system was analyzed at the nominal cruise condition ($M = 0.785$ at an altitude of 37,000 ft). For steady cruise, the net force over the entire aircraft is zero, which means the thrust created by the wing and tail propulsors must exactly balance the drag created by the rest of the airframe. A portion of the thrust is generated by the under-wing propulsors and another portion is generated by the aft-propulsor. Since the under-wing engines are not included in the aircraft model used in this work, the net force should be greater than zero. This computed net force value represents the net-thrust required from those engines to reach a steady condition.

One primary consideration in the STARC-ABL propulsion system design is what the optimal split between the under-wing and aft propulsors should be to achieve the lowest overall fuel consumption. A full aircraft design process addressing this question requires many considerations, such as thermodynamic performance, propulsion system weight, and aircraft center of gravity. In this work, we model only the thermodynamic performance of the aft-propulsor, and hence cannot fully address this design question. However, to account for the propulsor sizing and its effect on the overall aircraft performance, we consider optimized designs of BLI propulsors for three different sizes. The variations in the aft-propulsor inversely correlate with the under-wing engine sizing, and we therefore are able to draw some conclusions about the effect of propulsor sizing.

All optimizations were set up to minimize the shaft power required by the BLI propulsor at the cruise condition. The design variables consist of the fuselage and propulsor shape variables described in Sec. II.A, the angle of attack, and the applied BLI propulsor body force (i.e., the total force that would have been imparted to the flow by the fan in the real propulsor), for a total of 27 design variables. The complete problem is described in Table 1. The constraints consist of the cruise lift coefficient, 10 geometric thickness constraints, a minimum nozzle pressure ratio, and the target net force. The nozzle pressure ratio constraint is not normally used in fan design, but we employ it instead of a constraint on FPR because it was more well behaved in the shape optimization of the propulsor duct. The net force constraint is the most physically significant because it ultimately sizes the BLI propulsor. We ran two sets of optimizations: one with the distortion constraint ($\hat{\kappa}$) and one without. The value of the constraint on $\hat{\kappa}$ was derived empirically by finding the lowest

value that was achievable by the optimizer given the degrees of freedom it had available. When we tried lower values of $\hat{\kappa}$, the optimizations could not converge reliably for all power settings.

Table 1 Aeropropulsive design optimization problem.

	Variable or function	Description	Quantity
minimize	P_{BLI}	Shaft power required for the BLI propulsor	
with respect to	α	Angle of attack	1
	F_{BLI}	BLI propulsor body-force applied	1
	X_{shape}	Fuselage and propulsor nacelle shape variables	25
		Total	27
subject to	$C_L = 0.5$	Lift coefficient at cruise	1
	$0.99 \leq g_{\text{geo}} \leq 3.0$	Geometric thickness	10
	$\text{NPR} \geq 1.65$	Nozzle pressure ratio	1
	$F_{\text{net}} = F_{\text{net}}^*$	Required net force on the body	1
	$\hat{\kappa} \leq 0.035$	Aggregated distortion metric	1
		Total	14

We use the sign convention from the aerodynamic model, where the positive x -axis direction is defined from nose to tail. Using this convention, positive values of net force over the whole body represent a decelerating force on the body. Since the aerodynamic model excludes the under-wing propulsors, the F_{net} computed by this model represents a net decelerating force. On the real aircraft in steady flight, that decelerating force must be balanced by the thrust from the under-wing propulsors. In other words, a larger F_{net} corresponds to larger under-wing propulsors and a smaller aft-propulsor, and vice-versa.

Figure 8 shows the data dependencies between the different analyses in the fully coupled aeropropulsive optimization using an XDSM diagram [43]. The four analyses are coupled using OpenMDAO [28], which solves the nonlinear analysis and computes the total derivatives needed by the optimizer using a coupled-adjoint approach [46, 47]. The individual design feasible (IDF) MDO architecture is used to enforce the coupling [48].

The geometry engine used in this work is OpenVSP [30], which is integrated in the *ADflow* component. The *VSP Preprocessing* component shown in Fig. 8 is responsible for preparing the data for OpenVSP. OpenVSP exposes a number of parameters that control the shape and diameters of individual cross-sections on both the fuselage, BLI nacelle, and wing. However, for this work, a number of those parameters were linked together to provide a more physically meaningful geometry parameterization by defining a single global diameter parameter for the nacelle, as described in Sec. II.A. For example, the sharp trailing edge of the nacelle is parameterized with two separate diameters in the OpenVSP model: one for the upper surface and one for the lower surface. These two diameters have the same value so that the geometry stays water tight. This is accomplished via the *VSP Preprocessing* component in the model, which takes a set of design variables and relates them to the actual OpenVSP model inputs.

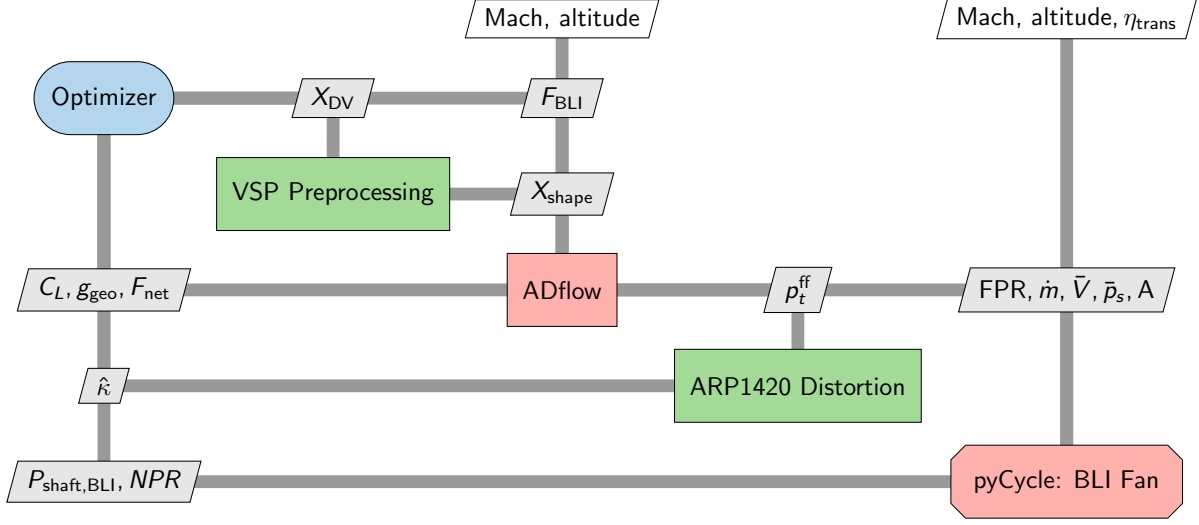


Fig. 8 XDSM diagram of the full optimization problem formulation. Green elements represent explicit calculations, while red elements represent implicit calculations; The red octagon indicates that “pyCycle: BLI Fan” has internal sub-models. The sub-models are shown in Fig. 7.

The *ARP1420 Distortion* component implements the distortion metric from the “Gas Turbine Engine Inlet Flow Distortion Guidelines” ARP1420 standard [49], using the scheme developed by Kenway and Kiris [6]. The metric captures the magnitude of the circumferential variation in total pressure across the fan face as

$$\kappa^i = \frac{\check{p}_t^{ff,i} - \bar{p}_t^{ff,i}}{\bar{p}_t^{ff,i}}, \quad (14)$$

where superscript ff denotes quantities taken at the fan face and superscript i denotes a specific radial ring of pressure measurements. There are two mean pressure values here: \bar{p}_t^{ff} is the overall mean total pressure and \check{p}_t^{ff} and is the total pressure averaged among all the values that are below \bar{p}_t^{ff} . These two metrics are illustrated in the right-hand side of Fig. 9, which shows a notional pressure trace taken at a single radial location.

In this model, we have five radial measurement locations with 30 sensors distributed evenly in the circumferential direction, yielding a total of 150 sensors, as shown on the left side of Fig. 9. The five distortion measurements from each of the five radii are aggregated with a KS function [50], which yields a smoothed maximum value ($\hat{\kappa}$) that can be used as a single additional constraint in the optimization:

$$\hat{\kappa} = \frac{1}{200} \ln \left[\sum_{i=0}^4 e^{200\kappa^i} \right]. \quad (15)$$

Our model quantifies some but not all of the adverse effects of distortion. High distortion levels can impact the inlet pressure recovery and also reduce fan efficiency. The inlet distortion effects are implicitly accounted for in the CFD

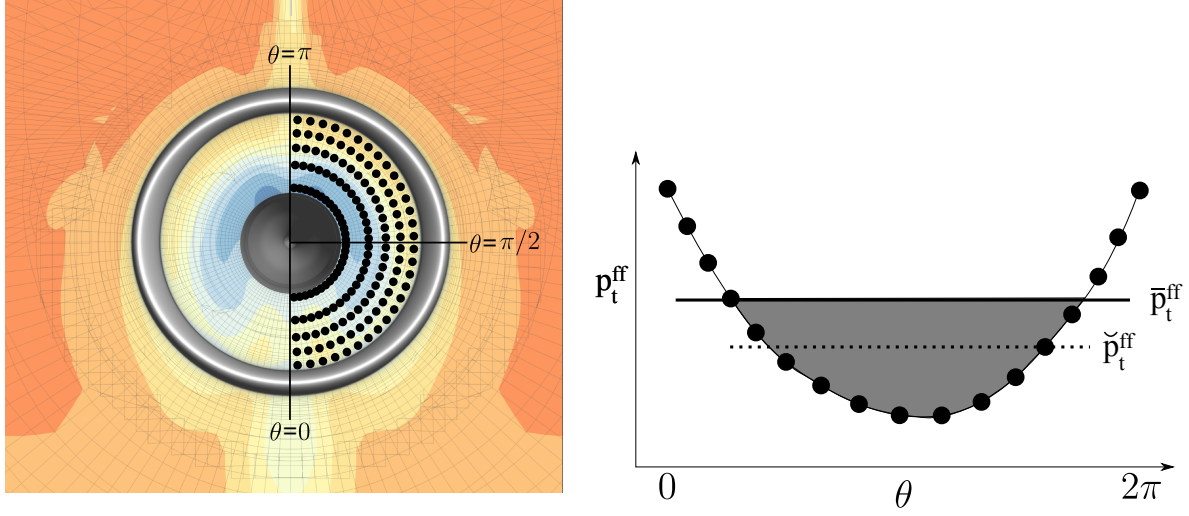


Fig. 9 ARP1420 distortion calculation diagram, showing the pressure rake locations (left) and a notional pressure trace taken across a single radial measurement stations (right).

simulation, which includes the inlet. Any loss of total pressure between the inlet highlight and the fan-face registers as a lower mass-averaged velocity at the fan-face, and is passed to the propulsion system via the aeropropulsive transfer scheme (discussed in Sec. III.A). On the other hand, the effect of distortion on fan efficiency was not considered in this work because no metric currently exists for this. Given the relatively low distortion levels in this aft-propulsor style configuration, we speculate that the fan efficiency effects would be minimal, but other configurations may require accounting for this effect.

B. Optimization Results

Three pairs of optimizations were performed for different thrust values, $F_{\text{net}}^* = \{9000, 11000, 13000\}$ N. These values were chosen so that the $F_{\text{net}}^* = 13000$ case (the smallest BLI propulsor) is close the 3500 hp (2610 kW) fan shaft power that was used in the original work by Welstead and Felder [11]. This was done to provide results that could be compared and used in future sizing studies. When normalized by freestream conditions and wing area, these forces correspond to a force coefficient of $C_F \times 10^4 = \{90.39, 110.5, 130.6\}$. As previously mentioned, two sets of optimizations were performed: one with the distortion constraint and another without.

The key performance metrics resulting from each optimization are listed in Table 2. The 9000 N case yields the largest aft-propulsor and hence requires the most shaft power. Compared to the 9000 N case, the 11000 N case requires 22% more thrust from the under-wing propulsors and uses 14.6% less shaft power for the BLI propulsor. The 13000 N case requires 44% more thrust from the under-wing propulsors and uses 29.2% less shaft power for the aft propulsor. In all three cases, the NPR constraint limits the FPR from going below 1.23.

The main conclusion from the data in Table 2 is that the impact of the distortion constraint on the BLI propulsor

Table 2 Optimization results for the 3-D STARC-ABL aeropropulsive optimization comparing unconstrained and distortion-constrained cases.

No κ constraint				Constrained κ		
$C_F \times 10^4$	FPR	κ ($\hat{\kappa}$)	P (kW)	FPR	κ ($\hat{\kappa}$)	ΔP (%)
90.39	1.233	0.0440 (0.0447)	3646.5	1.236	0.0300 (0.0350)	1.2
110.5	1.271	0.0426 (0.0434)	3177.9	1.308	0.0313 (0.0348)	0.9
130.6	1.286	0.0403 (0.0413)	2623.3	1.286	0.0312 (0.0350)	0.12

performance is always to reduce the effectiveness of the BLI propulsor and that the size of that reduction is a function of the propulsor diameter. The largest BLI propulsor ($C_F \times 10^4 = 90.39$) requires 1.2% more shaft power for the distortion constrained case to reach the same overall net force on the body compared the non constrained case. That case also had the highest distortion for the unconstrained optimization, which partially explains the large impact of the distortion constraint because it was effectively more restrictive. The largest propulsor ingests some of the freestream outside the boundary layer on the upper side of the aircraft fuselage, which contributes to the increased distortion in the unconstrained case.

These results may seem counterintuitive, since in a podded configuration lower distortion would typically lead to increased propulsor performance, yet the aeropropulsive BLI system shows the opposite trend. Recall that the reduction in distortion when the constraint is applied is achieved through changed so the aft fuselage and nacelle shape. These changes will impact not only inlet distortion, but also inlet performance (i.e. pressure recovery) and aerodynamic forces (i.e. pressure and viscous forces) as well. If inlet pressure recovery goes down or if fuselage or inlet drag goes up, then a larger propulsor is needed to achieve the net-zero force constraint and the required shaft power increases. It is possible that some of that increased power requirement could be mitigated by improved fan efficiency, however the impact of inlet distortion on fan efficiency (negative or positive) was not modeled in this work.

The trend of FPR vs. C_F is different for the unconstrained and distortion-constrained cases. For the unconstrained case, the optimal FPR increases monotonically, but that trend changes when the distortion constraint is applied. The distortion constraint was numerically challenging for the optimizer, and the $C_F \times 10^4 = 110.5$ case did not converge as tightly as the other cases—as evidenced by the slightly lower value of $\hat{\kappa}$.

We believe this to be a source of error that affected the final FPR value. The data from the other two cases indicates that lower values of $\hat{\kappa}$ are correlated with higher required shaft power and thus larger thrust contributions from the propulsor to satisfy the C_F constraint. Therefore, we hypothesize that a more tightly converged optimum would have been closer to the $\hat{\kappa}$ limit and would have yielded a slightly lower required shaft power.

Figure 10 shows the side and front views of the baseline and optimized geometries for the three F_{net}^* values. The color contours show the total pressure levels around the aircraft, where the front view contours highlight the distortion in the inlet for the BLI propulsors. In all three cases, some shaping on the nozzle plug also helps alleviate minor flow

separation, yielding slightly better overall performance. Compared to the baseline geometry, the nacelle walls are thicker near the leading edge and much thinner near the trailing edge compared to the baseline. The pressure contours also indicate that the flow is more uniform exiting the nozzle in the optimized cases.

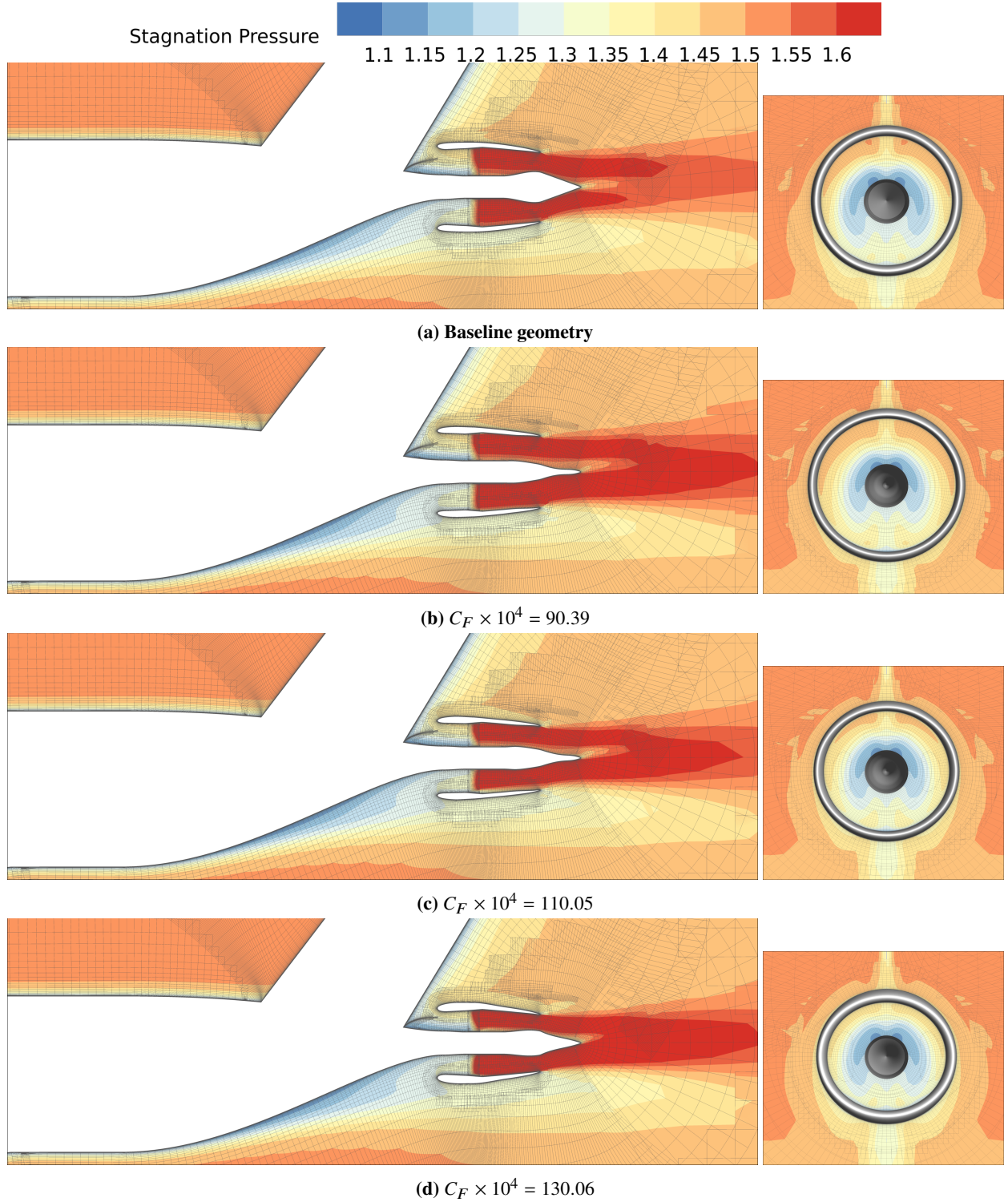


Fig. 10 Contours of stagnation pressure for the baseline and the three optimized geometries.

For all cases (baseline and three optimized geometries) we can see in the front-view that the fan-face has a zone of higher total pressure at the bottom position of the fan hub (i.e., at the zero degree position in Fig. 9) compared to all the other annular angles. As demonstrated by Kenway and Kiris [6], this annular non-uniformity is created primarily by the wing downwash induced at the tail. The wing downwash combined with the fuselage asymmetry also causes a gross imbalance in total pressure between the bottom and top positions at the fan tip. This creates a one-per-revolution excitation on the fan blades and that would require a careful design considering aeroelastic effects.

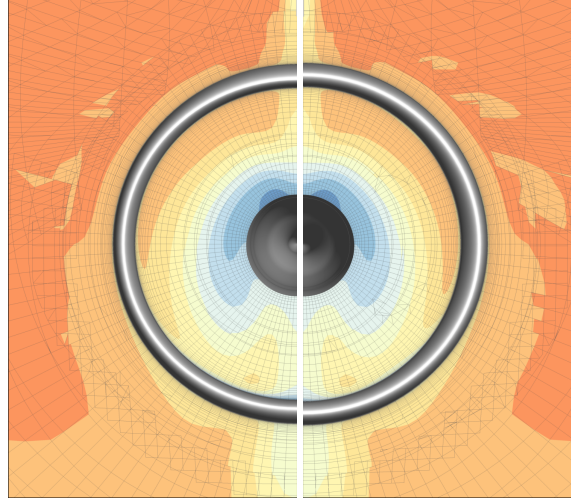
The second set of optimizations seeks to limit this circumferential distortion. The results of the distortion-constrained optimizations are shown in Fig. 11. These front views of the inlet highlight how the optimizer is able to restrict the distortion to the allowable levels. In all cases, the optimizer satisfied the overall constraint on the aggregated distortion ($\hat{\kappa}$), but because of the conservative nature of the KS function used to aggregate the actual maximum distortion [51, 52], (κ) is always slightly lower than the aggregated value.

Figure 11 shows consistent geometric trends between the three sets of cases. In all cases, the distortion-constrained inlet has an inlet profile thicker than the unconstrained one. The inlet lips tend to move radially outward as well, creating a sharper-lipped profile. The overall inlet diameters do not vary much between the constrained and unconstrained cases. The sharper-lipped inlets are a notable feature, since they may not perform well at other angles of attack.

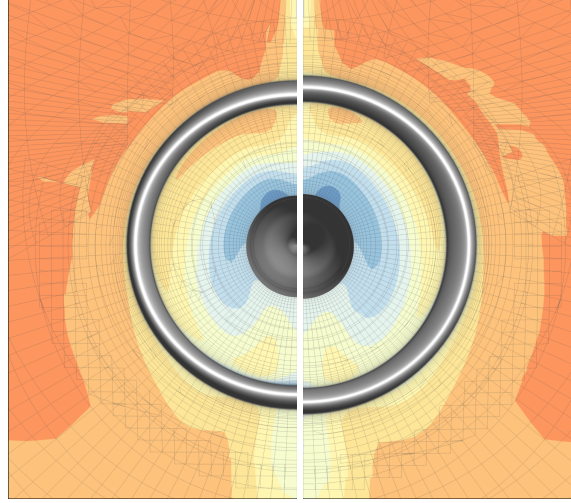
A more quantitative understanding of how the distortion constraint changes the inlet flow is shown in Figs. 13, 14, and 15, show the pressure along the sensor rake. The pressure rake positions are shown in Fig. 12, where the color of each sensor ring in Fig. 12 matches the pressure plots. In all three of these plots, the vast majority of the variation between the constrained and unconstrained designs shows up in the purple (r_4) radial pressure rake, which is closest to the fan tip. This makes sense because that rake shows the largest variation in total pressure around the annulus and hence it is the dominant contribution to the aggregated distortion constraint $\hat{\kappa}$. Given Eqn. 14, there are two ways that distortion can be reduced on any single annular ring in the propulsor: increase \check{p}_t^{ff} or decrease \bar{p}_t^{ff} . Both effects are present in the data. The $\hat{\kappa}$ constraint forces the optimizer to raise the total pressure around $\theta = 0$ which pulls up \check{p}_t^{ff} . It also lowers the total pressure in the neighborhood of $\theta = \pi/2$ which brings down \bar{p}_t^{ff} . Figures 13, 14, and 15 show a modest change in the total pressure distribution, which yields a 1%–1.5% reduction in maximum distortion for these three cases.

Another important trend that applies to all three propulsor sizes, is how the inner (r_0) and outer (r_4) rings have pressure signatures that are nearly 180 degrees out of phase with each other. In other words, the r_0 ring has a lower pressure at the same circumferential location that the r_4 ring has a high pressure. This trend is also shown in the qualitative results displayed in Fig. 10, but it is much more clearly seen in the pressure traces in Figs. 13, 14, and 15.

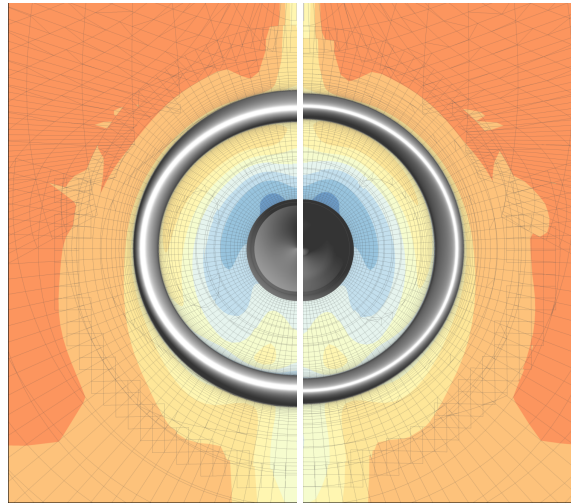
There is a smooth transition in phase angle between the rings as they progress farther outward, and the overall amplitude of the signal increases along the outward direction as well.



(a) $C_F \times 10^4 = 90.39$



(b) $C_F \times 10^4 = 110.05$



(c) $C_F \times 10^4 = 130.06$

Fig. 11 Comparison between the optimized designs for the unconstrained (left) and distortion-constrained (right) BLI propulsor inlet.

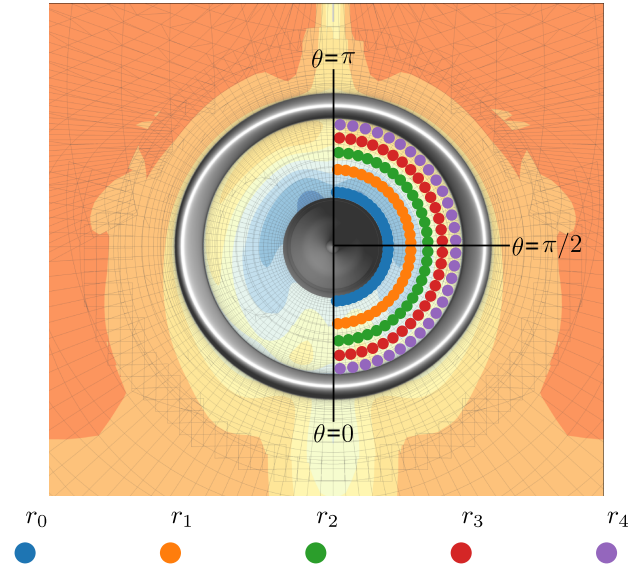


Fig. 12 Numerical pressure rake used to compute distortion metric, with 5 semicircular rings (r_0, \dots, r_4) consisting of 30 sensors each.

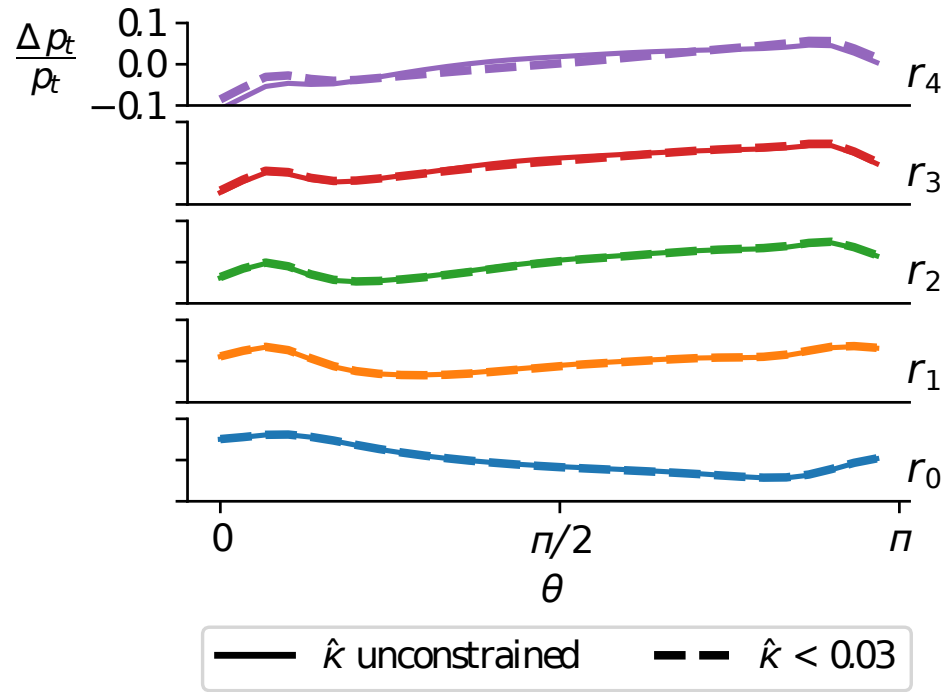


Fig. 13 $\Delta p_t / p_t$ for rakes r_0 – r_4 versus annular location (θ), for $C_F \times 10^4 = 90.39$.

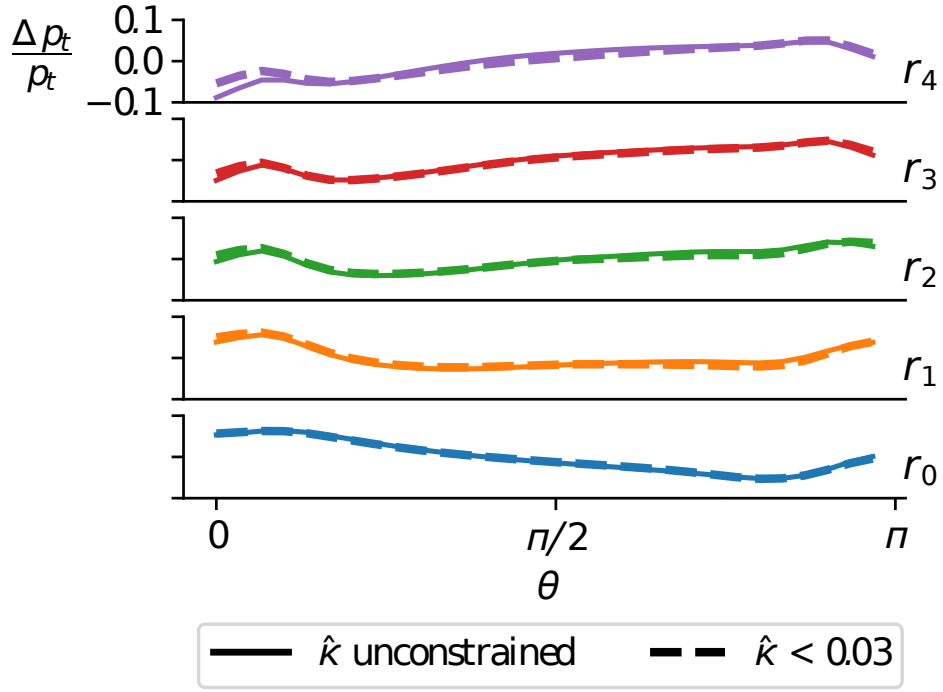


Fig. 14 $\Delta p_t/p_t$ for rakes r_0 – r_4 versus annular location (θ), for the $C_F \times 10^4 = 110.05$.

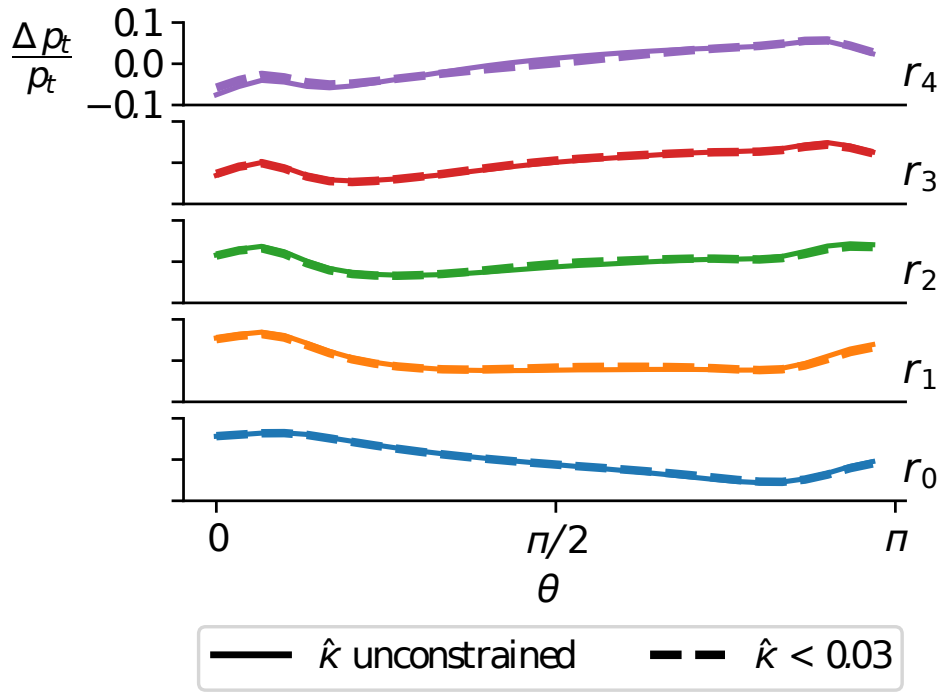


Fig. 15 $\Delta p_t/p_t$ for rakes r_0 – r_4 versus annular location (θ), for the $C_F \times 10^4 = 130.06$.

V. Conclusions

This study used design optimization of a coupled aeropropulsive model with 3-D RANS CFD aerodynamics to study the impact of a distortion constraint on the performance of three different BLI propulsor sizes for the STARC-ABL aircraft configuration. The aeropropulsive model used a novel coupling strategy that combined a body-force zone to predict propulsor thrust with a 1-D thermodynamic cycle model to predict propulsor power usage. Three propulsors corresponding to different fractions of total thrust were optimized, resulting in three different propulsor sizes. The results show that, due to aeropropulsive coupling, the distortion constraint reduces the performance of each propulsor by different amounts. This underscores both the importance of using fully-coupled aeropropulsive models for the design of BLI propulsion systems and the need to employ 3-D RANS models to accurately size BLI systems.

Six separate aeropropulsive optimizations were run: two sets of cases—with and without a distortion constraint—for three different propulsor sizes. These results compare cases with and without distortion at the same net force on the overall body, providing the required results to examine how BLI propulsor design is affected by inlet distortion constraints. The results show that changing the shape of the aft fuselage and inlet in an aeropropulsive optimization can satisfy a distortion constraint for the STARC-ABL configuration. By extension, it is reasonable to assume that this technique can be used for other tail-cone-thruster configurations that exhibit similar flow fields. However, it was not possible to reduce the distortion metric below 0.03 for this geometric parameterization. Future work should examine if a more flexible design parameterization would have enabled lower values for the constraint.

Given the current uncertainty associated with how much performance impact high levels of distortion have on fan performance, the ability to limit that distortion via aerodynamic shaping offers an alternate route to limiting its adverse impact. However, satisfying the distortion constraint came at the cost of a reduced power saving coefficient. Imposing a distortion constraint causes an increase in the required propulsor shaft power relative to the unconstrained case. This effect can be interpreted as an increase in nacelle drag for the distortion-constrained case, which required a slightly larger amount of shaft power to meet the net-zero force constraint. The magnitude of that increase varies from 0.12% to 1.2% between the smallest propulsor and largest one. The variation in the impact of the distortion constraint with respect to the propulsor size is one of the primary contributions of this work. At the conceptual design stage, it might be tempting to apply a constant knock-down factor—selected based on the CFD analysis of a baseline configuration—to account for distortion effects on a particular concept. However, this data shows that using a constant knock-down for an aft-mounted propulsor configuration could result in a strong under or over penalization, depending on which size propulsor is chosen as the baseline.

Regardless of the specific value for the impact of the distortion constraint, the impact always competed with the BLI efficiency gains. This poses a dilemma for future BLI system designs. The purpose of the distortion constraint is to ensure that the fan adiabatic efficiency can be maintained, and to reduce the structural loads on the blades so that the fan remains lightweight. However, if imposing that constraint makes the aeropropulsive system less efficient, then it may be

preferable to accept a small penalty in fan efficiency or increased fan weight rather than design for lower distortion. The best tradeoff between efficiency and distortion ultimately depends on the specifics of the actual system being considered. Even within the context of a single aircraft configuration, such as the STARC-ABL, the size of the aft propulsor will influence the tradeoff.

This work represents the first fully-coupled aeropropulsive optimization for the design of BLI propulsion systems that includes both aerodynamic and propulsion design variables. It is also the first aeropropulsive design optimization using a 3-D RANS model that directly considers the impact of propulsor sizing. There remains much more work to be done in this area, especially with regard to considering more operating conditions (on design and off design) in the optimization. The off-design analysis for the propulsion model will present a significant new challenge because the inputs to the model will change and will require tighter coupling between the aerodynamic and structural models. Despite these challenges, the aeropropulsive coupling approach presented in this paper provides a foundation for more realistic multipoint optimizations.

Acknowledgments

The authors would like to acknowledge Bret Naylor, Kenneth Moore, and the rest of the NASA Glenn OpenMDAO development team, who have spent countless hours building the framework that has enabled this research. We would also like to thank James Felder, of the NASA Glenn Research Center, for lending his time and expertise to many discussions regarding the propulsion system design of the STARC-ABL configuration. We also gratefully acknowledge NASA's Aeronautics Research Mission Directorate Transformational Tools and Technologies (TTT) and the Advanced Air Transport Technologies (AATT) projects for their continued support of this work.

References

- [1] Smith, A. M. O., and Roberts, H. E., “The Jet Airplane Utilizing Boundary Layer Ingestion for Propulsion,” *Journal of Aeronautical Sciences*, Vol. 14, No. 2, 1947, pp. 97–109.
- [2] Wislicenus, G. F., “Hydrodynamics and Propulsion of Submerged Bodies,” *Journal of the American Rocket Society*, Vol. 30, 1960, pp. 1140–1148.
- [3] Gearhart, W. S., and Henderson, R. E., “Selection of a Propulsor for a Submersible System,” *Journal of Aircraft*, Vol. 3, No. 1, 1966, pp. 84–90.
- [4] Smith, L. H., “Wake Ingestion Propulsion Benefit,” *Journal of Propulsion and Power*, Vol. 9, No. 1, 1993, pp. 74–82. doi:10.2514/6.1991-2007.
- [5] Ordaz, I., Rallabhandi, S. K., Nielsen, E. J., and Diskin, B., “Mitigation of Engine Inlet Distortion through Adjoint-Based Design,” *35th AIAA Applied Aerodynamics Conference*, 2017, p. 3410. doi:10.2514/6.2017-3410, aIAA-2017-3410.
- [6] Kenway, G. K., and Kiris, C. C., “Aerodynamic Shape Optimization of the STARC-ABL Concept for Minimal Inlet Distortion,” *AIAA/ASCE/AHS/ASC Structures, Structural Dynamics, and Materials Conference*, American Institute of Aeronautics and Astronautics, 2018. doi:10.2514/6.2018-1912.
- [7] Hirt, S. M., Arend, D. J., Wolter, J. D., and Johnson, A., “Development of a Flow Field for Testing a Boundary-Layer Ingesting Propulsor,” *AIAA Propulsion and Energy Forum*, 2017. doi:10.2514/6.2017-5043.
- [8] Arend, D. J., Wolter, J. D., Hirt, S. M., Provenza, A., Gazzaniga, J. A., Cousins, W. T., Hardin, L. W., , and Sharma, O., “Experimental Evaluation of an Embedded Boundary Layer Ingesting Propulsor for Highly Efficient Subsonic Cruise Aircraft,” *53rd AIAA/SAE/ASEE Joint Propulsion Conference*, 2017. AIAA-2017-5041.
- [9] Hardin, L. W., Cousins, W. T., Wolter, J. D., Arend, D. J., and Hirt, S. M., “Data Analysis Techniques for Fan Performance in Highly-Distorted Flows from Boundary Layer Ingesting Inlets,” *2018 AIAA Aerospace Sciences Meeting*, 2018. doi:10.2514/6.2018-1888.
- [10] Provenza, A. J., Duffy, K. P., and Bakhle, M. A., “Aeromechanical Response of a Distortion Tolerant Boundary Layer Ingesting Fan,” *ASME Turbo Expo 2018: Turbomachinery Technical Conference and Exposition*, 2018. doi:10.1115/GT2018-77094.
- [11] Welstead, J., and Felder, J. L., “Conceptual Design of a Single-Aisle Turboelectric Commercial Transport with Fuselage Boundary Layer Ingestion,” *54th AIAA Aerospace Sciences Meeting*, American Institute of Aeronautics and Astronautics, 2016. doi:10.2514/6.2016-1027.
- [12] Betz, A., *Introduction to the Theory of Flow Machines*, Pergamon Press, Oxford, UK, 1966.
- [13] Drela, M., “Power Balance in Aerodynamic Flows,” *AIAA Journal*, Vol. 47, No. 7, 2009, pp. 1761–1771. doi:10.2514/1.42409.
- [14] Daggett, D. L., Kawai, R., , and Friedman, D., “Blended Wing Body Systems Studies: Boundary Layer Ingestion Inlets With Active Flow Control,” Tech. Rep. NASA/CR-2003-212670, NASA Langley Research Center, December 2003.

- [15] Felder, J. L., Kim, H. D., and Brown, G. V., “Turboelectric Distributed Propulsion Engine Cycle Analysis for Hybrid-Wing-Body Aircraft,” *47th AIAA Aerospace Sciences Meeting including The New Horizons Forum and Aerospace Exposition*, 2009. doi:10.2514/6.2009-1132, aIAA 2009-1132.
- [16] Felder, J. L., Brown, G. V., Kim, H. D., and Chu, J., “Turboelectric Distributed Propulsion in a Hybrid Wing Body Aircraft,” *International Symposium on Air Breathing Engines 2011*, 2011.
- [17] Drela, M., “Development of the D8 Transport Configuration,” *29th AIAA Applied Aerodynamics Conference*, American Institute of Aeronautics and Astronautics, 2011. doi:10.2514/6.2011-3970.
- [18] Liu, C., Doulgeris, G., Laskaridis, P., and Singh, R., “Thermal cycle analysis of turboelectric distributed propulsion system with boundary layer ingestion,” *Aerospace Science and Technology*, Vol. 27, No. 1, 2013, pp. 163–170. doi:10.1016/j.ast.2012.08.003.
- [19] Laskaridis, P., Pachidis, V., and Pilidis, P., “Opportunities and challenges for distributed propulsion and boundary layer ingestion,” *Aircraft Engineering and Aerospace Technology*, Vol. 86, No. 6, 2014, pp. 451–458. doi:10.1108/AEAT-05-2014-0067.
- [20] Uranga, A., Drela, M., Hall, D. K., and Greitzer, E. M., “Analysis of the Aerodynamic Benefit from Boundary Layer Ingestion for Transport Aircraft,” *AIAA Journal*, Vol. 0, No. 0, 2018, pp. 1–11. doi:10.2514/1.J056781.
- [21] Hendricks, E. S., “A Review of Boundary Layer Ingestion Modeling Approaches for use in Conceptual Design,” NASA Technical Memorandum NASA/TM—2018-219926, NASA Glenn Research Center, Cleveland OH, July 2018.
- [22] Gray, J. S., Mader, C. A., Kenway, G. K. W., and Martins, J. R. R. A., “Modeling Boundary Layer Ingestion Using a Coupled Aeropropulsive Analysis,” *Journal of Aircraft*, Vol. 55, No. 3, 2018, pp. 1191–1199. doi:10.2514/1.C034601.
- [23] Gray, J. S., and Martins, J. R. R. A., “Coupled Aeropropulsive Design Optimization of a Boundary-Layer Ingestion Propulsor,” *The Aeronautical Journal*, Vol. 123, No. 1259, 2019, pp. 121–137. doi:10.1017/aer.2018.120.
- [24] Bowman, C. L., Felder, J. L., and Marien, T. V., “Turbo- and Hybrid-Electrified Aircraft Propulsion Concepts for Commercial Transport,” *2018 AIAA/IEEE Electric Aircraft Technologies Symposium (EATS)*, 2018. doi:10.2514/6.2018-4984.
- [25] Hall, D. K., Dowdle, A., Gonzalez, J., Trollinger, L., and Thalheimer, W., “Assessment of a Boundary Layer Ingesting Turboelectric Aircraft Configuration using Signomial Programming,” *2018 Aviation Technology, Integration, and Operations Conference, AIAA AVIATION Forum*, 2018. doi:10.2514/6.2018-3973, aIAA 2018-3973.
- [26] Rodriguez, D. L., “A multidisciplinary optimization method for designing boundary layer ingesting inlets,” Ph.D. thesis, Stanford University, Stanford, CA, 2001.
- [27] Rodriguez, D. L., “Multidisciplinary optimization method for designing boundary layer ingesting inlets,” *Journal of Aircraft*, Vol. 46, No. 3, 2009, pp. 883–894. doi:10.2514/1.38755.
- [28] Gray, J. S., Hwang, J. T., Martins, J. R. R. A., Moore, K. T., and Naylor, B. A., “OpenMDAO: An open-source framework for multidisciplinary design, analysis, and optimization,” *Structural and Multidisciplinary Optimization*, Vol. 59, No. 4, 2019, pp. 1075–1104. doi:10.1007/s00158-019-02211-z.

- [29] Hall, D. K., Greitzer, E. M., and Tan, C. S., "Analysis of Fan Stage Conceptual Design Attributes for Boundary Layer Ingestion," *Journal of Turbomachinery*, Vol. 139, No. 7, 2017, pp. 071012–071012–10. doi:10.1115/1.4035631.
- [30] Hahn, A., "Vehicle Sketch Pad: A Parametric Geometry Modeler for Conceptual Aircraft Design," *48th AIAA Aerospace Sciences Meeting Including the New Horizons Forum and Aerospace Exposition*, American Institute of Aeronautics and Astronautics, 2010. doi:10.2514/6.2010-657.
- [31] Secco, N. R., Jasa, J. P., Kenway, G. K. W., and Martins, J. R. R. A., "Component-based Geometry Manipulation for Aerodynamic Shape Optimization with Overset Meshes," *AIAA Journal*, Vol. 56, No. 9, 2018, pp. 3667–3679. doi:10.2514/1.J056550.
- [32] Mader, C. A., Kenway, G. K. W., Yildirim, A., and Martins, J. R. R. A., "ADflow—An open-source computational fluid dynamics solver for aerodynamic and multidisciplinary optimization," *Journal of Aerospace Information Systems*, (In press).
- [33] Yildirim, A., Kenway, G. K. W., Mader, C. A., and Martins, J. R. R. A., "A Jacobian-free approximate Newton–Krylov startup strategy for RANS simulations," *Journal of Computational Physics*, Vol. 397, 2019, p. 108741. doi:10.1016/j.jcp.2019.06.018.
- [34] Kenway, G. K. W., Mader, C. A., He, P., and Martins, J. R. R. A., "Effective Adjoint Approaches for Computational Fluid Dynamics," *Progress in Aerospace Sciences*, Vol. 110, 2019, p. 100542. doi:10.1016/j.paerosci.2019.05.002.
- [35] Chan, W. M., "Advances in Software Tools for Pre-processing and Post-processing of Overset Grid Computations," *9th International Conference on Numerical Grid Generation in Computational Field Simulations*, 2005.
- [36] Gong, Y., "A Computational Model for Rotating Stall and Inlet Distortion in Multistage Compressor," Ph.D. thesis, Massachusetts Institute of Technology, Cambridge, MA, 1999.
- [37] Hsiao, E., Naimi, M., d Jeffrey P. Lewis, Dalbey, K., Gong, Y., and Tan, C., "Actuator Duct Model of Turbomachinery Components for Powered-Nacelle Navier-Stokes Calculations," *JOURNAL OF PROPULSION AND POWER*, Vol. 17, No. 4, 2001. doi:10.2514/2.5825.
- [38] Livesey, J. L., and Hugh, T., "'Suitable Mean Values' in One-Dimensional Gas Dynamics," *Journal of Mechanical Engineering Science*, Vol. 8, No. 4, 1966, pp. 374–383. doi:10.1243/JMES_JOUR_1966_008_049_02.
- [39] Livesey, J. L., "Flow property averaging methods for compressible internal flows," *AIAA 20th Aerospace Sciences Meeting*, 1982. doi:10.2514/6.1982-135.
- [40] Gray, J. S., Chin, J., Hearn, T., Hendricks, E., Lavelle, T., and Martins, J. R. R. A., "Chemical Equilibrium Analysis with Adjoint Derivatives for Propulsion Cycle Analysis," *Journal of Propulsion and Power*, Vol. 33, No. 5, 2017, pp. 1041–1052. doi:10.2514/1.B36215.
- [41] Hearn, T. A., Hendricks, E., Chin, J., and Gray, J. S., "Optimization of Turbine Engine Cycle Analysis with Analytic Derivatives," *17th AIAA/ISSMO Multidisciplinary Analysis and Optimization Conference*, American Institute of Aeronautics and Astronautics, 2016. doi:10.2514/6.2016-4297.

- [42] Hendricks, E. S., and Gray, J. S., “pyCycle: A Tool for Efficient Optimization of Gas Turbine Engine Cycles,” *Aerospace*, Vol. 6, No. 87, 2019. doi:10.3390/aerospace6080087.
- [43] Lambe, A. B., and Martins, J. R. R. A., “Extensions to the Design Structure Matrix for the Description of Multidisciplinary Design, Analysis, and Optimization Processes,” *Structural and Multidisciplinary Optimization*, Vol. 46, 2012, pp. 273–284. doi:10.1007/s00158-012-0763-y.
- [44] “U.S. Standard Atmosphere, 1976,” NASA Technical Memorandum NASA-TM-X-74335, NOAA-S/T-76-1562, NASA, Washington DC, USA, Octobe 1976.
- [45] Jones, S. M., Haller, W. J., and Tong, M. T., “An N+3 Technology Level Reference Propulsion System,” Tech. rep., NASA Glenn Research Center, 2017. NASA/TM—2017-219501.
- [46] Martins, J. R. R. A., and Hwang, J. T., “Review and Unification of Methods for Computing Derivatives of Multidisciplinary Computational Models,” *AIAA Journal*, Vol. 51, No. 11, 2013, pp. 2582–2599. doi:10.2514/1.J052184.
- [47] Hwang, J. T., and Martins, J. R. R. A., “A computational architecture for coupling heterogeneous numerical models and computing coupled derivatives,” *ACM Transactions on Mathematical Software*, Vol. 44, No. 4, 2018, p. Article 37. doi:10.1145/3182393.
- [48] Martins, J. R. R. A., and Lambe, A. B., “Multidisciplinary Design Optimization: A Survey of Architectures,” *AIAA Journal*, Vol. 51, No. 9, 2013, pp. 2049–2075. doi:10.2514/1.J051895.
- [49] SAE S-16 Committee, “Gas turbine inlet flow distortion guidelines,” Tech. Rep. ARP1420C, Society of Automotive Engineers, April 2017.
- [50] Kreisselmeier, G., and Steinhauser, R., “Systematic Control Design by Optimizing a Vector Performance Index,” *International Federation of Active Controls Symposium on Computer-Aided Design of Control Systems, Zurich, Switzerland*, 1979. doi:10.1016/S1474-6670(17)65584-8.
- [51] Poon, N. M. K., and Martins, J. R. R. A., “An Adaptive Approach to Constraint Aggregation Using Adjoint Sensitivity Analysis,” *Structural and Multidisciplinary Optimization*, Vol. 34, No. 1, 2007, pp. 61–73. doi:10.1007/s00158-006-0061-7.
- [52] Lambe, A. B., Martins, J. R. R. A., and Kennedy, G. J., “An Evaluation of Constraint Aggregation Strategies for Wing Box Mass Minimization,” *Structural and Multidisciplinary Optimization*, Vol. 55, No. 1, 2017, pp. 257–277. doi:10.1007/s00158-016-1495-1.